Monthly Notices
of the
ROYAL ASTRONOMICAL SOCIETY

Mon. Not. R. Astron. Soc. **417,** 1839–1852 (2011) doi:10.1111/j.1365-2966.2011.19371.x

The properties of pre-stellar discs in isolated and multiple pre-stellar systems

T. Hayfield,[1,2⋆] L. Mayer,[3] J. Wadsley[4] and A. C. Boley[5]

[1]*Physics Department, Institute of Astronomy, ETH Zürich, Wolfgang-Pauli-Strasse 27, CH–8093 Zürich, Switzerland*
[2]*Max-Planck-Institut für Astronomie, Königstuhl 17, D-69117 Heidelberg, Germany*
[3]*Institute of Theoretical Physics, University of Zürich, Winterthurerstrasse 190, CH–8057 Zürich, Switzerland*
[4]*Department of Physics & Astronomy, McMaster University, 1280 Main Street West, Hamilton, ON L8S 4M1, Canada*
[5]*Astronomy Department, University of Florida, 211 Bryant Space Science Center, PO Box 112055, Gainesville, FL 32611-2055, USA*

Accepted 2011 July 2. Received 2011 June 24

ABSTRACT

We present high-resolution 3D smoothed particle hydrodynamics simulations of the formation and evolution of protostellar discs in a turbulent molecular cloud. Using a piecewise polytropic equation of state, we perform two sets of simulations. In both cases, we find that isolated systems undergo a fundamentally different evolution than members of binary or multiple systems. When formed, isolated systems must accrete mass and increase their specific angular momentum, leading to the formation of massive, extended discs, which undergo strong gravitational instabilities and are susceptible to disc fragmentation. Fragments with initial masses of 5.5, 7.4 and 12 $M_{\rm jup}$ are produced in our simulations. In binaries and small clusters, we observe that due to competition for material from the parent core, members do not accrete significant amounts of high specific angular momentum gas relative to isolated systems. We find that discs in multiple systems are strongly self-gravitating but that they are stable against fragmentation due to disc truncation and mass profile steeping by tides, accretion of high specific angular momentum gas by other members and angular momentum being redirected into members' orbits. In general, we expect disc fragmentation to be less likely in clusters and to be more a feature of isolated systems.

Key words: gravitation – instabilities – protoplanetary discs – stars: formation – planetary systems.

1 INTRODUCTION

The overall paradigm under which star formation occurs remains under debate. One hypothesis is that stars are thought to form as a collection of low-mass fragments in collapsing clumps of gas, and then undergo *competitive accretion* as the fragments try to accrete gas from their common reservoir (Bonnell et al. 2001; Bonnell & Bate 2006). The main competing hypothesis is *gravitational collapse*, where massive star-forming clumps collapse and form multiple cores. Each star forms from the gas that is available in its own core, with limited accretion from other material in the parent clump (Krumholz, McKee & Klein 2005). Regardless of the star formation paradigm, in the case of solar-type stars, the end result is most likely membership in a binary or multiple system (Duquennoy & Mayor 1991; Eggenberger, Udry & Mayor 2004). Scenarios for the formation of such systems abound. Amongst the simplest, most idealized scenarios are the fission of a bar-unstable core (Durisen et al. 1986; Burkert, Bate & Bodenheimer 1997) and the fragmentation of centrally condensed, rotating, magnetized cores (Boss 1997a). More complicated hypotheses appeal to the chaos of the cloud environment, such as core–core collisions (Turner et al. 1995), protostellar encounters (Shen et al. 2010), dynamical capture in unstable multiple systems (Bate, Bonnell & Bromm 2002) and accretion-triggered fragmentation (Bonnell 1994; Whitworth et al. 1995; Hennebelle et al. 2004; Offner, Klein & McKee 2008; Kratter, Murray-Clay & Youdin 2010).

Star formation scenarios involving the rapid collapse of a protostellar core following the loss of support against gravity require the formation of a massive accretion disc around the central object (e.g. Vorobyov & Basu 2007; Walch et al. 2010). Such discs undergo a short-lived ∼0.1 Myr stage where the disc is massive relative to its host ($0.1 < M_{\rm d}/M_{\star} < 1$) and where gravitational instabilities operate to transport mass through the disc on to the central protostar (Vorobyov & Basu 2007). Massive, accreting and extended protostellar discs have been shown to be susceptible to fragmentation, which could be responsible for a range of phenomena such as FU Orionis events and early dust processing if the clumps are disrupted (Boley et al. 2010; Nayakshin 2010), and the formation of substellar companions otherwise (Vorobyov & Basu 2007; Boley 2009).

⋆E-mail: hayfield@mpia.de

Given the problem that both the standard core accretion planet formation time-scale and protostellar disc lifetimes are typically a few Myr (Haisch, Lada & Lada 2001), the idea of creating giant planets in a few orbital times via gravitational instabilities was revived (Boss 1997b) and has since been the subject of sustained interest (Pickett et al. 2000; Boss 2002, 2008; Mayer et al. 2004, 2007; Pickett & Durisen 2007; Boley et al. 2006; Boley 2009). Analytical works constraining inner disc fragmentation (Rafikov 2005, 2007) and the short cooling times required to form long-lived clumps within ∼10 au in simulations of protoplanetary discs, along with observations of massive planets on wide orbits (e.g. Marois et al. 2008, 2010), have led to a shift in focus to outer disc (>40 au) fragmentation (e.g. Stamatellos, Hubber & Whitworth 2007; Boley 2009; Dodson-Robinson et al. 2009; Vorobyov & Basu 2010). Whether the extended disc models used in these studies are similar to discs formed from collapsed molecular cloud cores remains to be seen.

In the light of the likely connection between outer disc fragmentation and early protostellar systems, we examine in this paper the formation of discs in detail using 3D smoothed particle hydrodynamics (SPH) simulations of core collapse in turbulent molecular clouds. In particular, we compare the early evolution in mass, surface density, specific angular momentum and disc stability between several different systems under near-identical conditions. In one set of simulations, we compare an isolated and a binary system, and in the other we compare an isolated system and a small cluster. Previous studies of gravitational instabilities in binary systems have yielded mixed results, with some finding that the perturbing companion hinders fragmentation through disc truncation and tidal heating (Nelson 2000; Mayer et al. 2005) and alternatively promotes fragmentation, also through tidal perturbations (Boss 2006). However, the evolved systems considered in these studies may not be as susceptible to fragmentation as their protobinary counterparts, which we investigate here, due to the enhanced importance of gravitational instabilities during protostellar disc formation.

The paper is laid out as follows. In Section 2, we discuss the simulations, initial conditions (ICs) and the clump identification procedure. In Section 3, we present the results and analysis. Further discussion is provided in Section 4, and our conclusions are laid out in Section 5.

2 THE SIMULATIONS

All calculations were run with GASOLINE (Wadsley, Stadel & Quinn 2004), a parallel implementation of TreeSPH. We employ a fixed number N of smoothing neighbours, with the main runs using $N = 32$. Artificial viscosity is the standard prescription (Gingold & Monaghan 1983) with $\alpha = 1$, $\beta = 2$, controlled with a Balsara switch (Balsara 1989).

2.1 Initial conditions

The cloud in this experiment is spherical and uniform with a radius of 0.188 pc, a mass of 50 $M_\odot$ and a temperature of 10 K, as in Bate, Bonnell & Bromm (2003). It was seeded with supersonic turbulent velocities and is marginally self-bound. To simulate interstellar turbulence, the velocity field of the cloud was generated on a grid as a divergence-free Gaussian random field with an imposed power spectrum $P(k) \propto k^{-4}$. The resulting velocity dispersion $\sigma(l)$ varies as $l^{1/2}$ and is consistent with the Larson scaling relations (Larson 1981). The velocities were then interpolated from the grid to the particles. Finally, the condition that the cloud be marginally self-bound gives a normalization for the global velocity dispersion of 1.17 km s^{-1}. We describe the results of two simulations in this paper, run A and run B. Runs A and B are different random realizations of the same ICs, with the same power spectrum, but with different initial phases of the velocity field. As a result, the first objects that form in run A (which are the only ones that we can follow owing to the high computational expense of modelling hydrodynamics at high resolution without employing sinks) are different from those in run B. In run A, we have two subsimulations, one in which a binary system naturally arises and another in which we suppress the production of the secondary. We then compare the subsequent evolution of the systems in an otherwise identical core and cloud environment. In run B, an isolated system and a cluster are produced roughly coevally at opposing ends of a filamentary structure. We compare the evolution in these systems, having been produced in similar environments.

2.1.1 Run A: the isolated and binary systems

We describe here how we produced the isolated system in run A. The fiducial cloud free-fall time is given by $t_{\rm ff} = \sqrt{3\pi/32 G\rho_{\rm cl}} = 1.92 \times 10^5$ yr, with $\rho_{\rm cl} = 1.2 \times 10^{-19}$ g cm^{-3} being the initial cloud density. The evolution of the cloud was followed up to $t = 1.2\,t_{\rm ff}$.

At $t = 0.88\,t_{\rm ff}$, a core, whose collapse we follow in detail, has already formed a small central protostar. The protostar accretes rapidly via a connecting filament until the filament itself produces a fragment. The fragment survives first pericentre with the protostar and becomes a companion.

We produced an isolated system for comparison under near-identical conditions by tracing the particles comprising the companion back in time to $t = 0.88\,t_{\rm ff}$ and stirring them by randomly exchanging their velocities. This procedure conserves the energy and linear momentum but not the angular momentum of the stirred particles. There were approximately 5300 particles, totalling 0.053 $M_\odot$, that had their velocities perturbed.

2.2 Thermodynamics

We model the thermodynamics of collapse with a piecewise polytropic equation of state (EOS; Tohline 1982; Bate 1998):

$$P = \begin{cases} \kappa_0 \rho & \rho < 10^{-13}, \\ \kappa_1 \rho^{7/5} & 10^{-13} \leq \rho, \end{cases} \quad (1)$$

with κ_0 chosen so that the sound speed $c_{\rm s} = 1.84 \times 10^4$ cm s^{-1} and the subsequent κ_1 chosen to ensure pressure continuity. Theoretical estimates of temperatures in molecular clouds find that their temperatures should range between 5–10 K over densities ranging from 10^{-19} to 10^{-13} g cm^{-3} (Low & Lynden-Bell 1976; Larson 1985; Masunaga & Inutsuka 2000). Observations indicate a somewhat higher minimum temperature of 8 K, with typical temperatures of 10–13 K (Kirk, Ward-Thompson & André 2007). The EOS thus captures the approximately isothermal behaviour of the cloud in the intermediate density regime. At high densities, the gas transitions to being adiabatic with exponent $\gamma = 7/5$. This EOS is a simplification of the internal heating and cooling processes in a molecular cloud and, in the high-density regime, will minimize the potential for fragmentation. Furthermore, through our choice of softening ($\epsilon_{\rm g} = 2.3$ au) combined with the polytropic EOS, we allow the first hydrostatic core to be marginally resolved while still inhibiting its subsequent dissociating collapse (Larson 1969), which can

be computationally demanding to resolve. 3D collapse simulations with more sophisticated thermodynamics, and including radiative transfer, but of isolated cores with no turbulent cloud environment, have been performed by Whitehouse & Bate (2006), Bate (2010), Tomida et al. (2010) and Commerçon et al. (2010). While proper treatments of both thermodynamics and radiative transfer are important, such simulations are computationally expensive and so far can only be carried out at lower resolution and with shorter integration times than required in our calculations. We shall explore the problem with more detailed thermodynamics and radiative transfer in a future publication. We reiterate, though, that the early evolution of protostellar discs and protobinaries is still not understood. Before the complexities of radiation hydrodynamics can be introduced, the birth of these systems must be understood through examination of high-resolution hydrodynamics simulations with a reasonable, albeit simplified, EOS, which is the focus of this paper.

2.3 Resolution

The simulations employ 5×10^6 particles. The particle masses m_p are thus $1.0 \times 10^{-5}\,\mathrm{M}_\odot$ in all simulations. The minimum jeans mass M_j, defined as $M_\mathrm{j} = 2.92\,c_\mathrm{s}^3/(G^{3/2}\rho_0^{1/2})$, is that obtained at the transition density to the adiabatic EOS, and is $M_\mathrm{j}^* = 1.7 \times 10^{-3}\,\mathrm{M}_\odot = 1.8\,M_\mathrm{jup}$. Previous work has shown that molecular clouds should have a minimum jeans mass (Low & Lynden-Bell 1976), with the gas becoming optically thick to its own cooling radiation at $\sim 10^{-13}\,\mathrm{g\,cm^{-3}}$. In our 5×10^6 particle runs, $M_\mathrm{j}^*/m_\mathrm{p} = 167$ and the jeans mass remains adequately resolved at all times. A fixed gravitational softening $\epsilon_\mathrm{g} = 2.3\,\mathrm{au}$ is used in all simulations.

2.4 Disc identification

In order to compare and separate the systems in the simulations, a working definition of what comprises a protostellar system is required. We define a protostellar system within this context as being a self-bound gas structure with a peak density greater than $6.7 \times 10^{-12}\,\mathrm{g\,cm^{-3}}$. The density threshold was chosen to be well above the critical density in order to identify only bound structures that are in the adiabatic regime. To determine whether any cold, isothermal gas is bound to a given system, we require that it is bound below a threshold binding energy $E_\mathrm{b} = 2.6 \times 10^{34}\,\mathrm{erg}$. The binding energy criterion is imposed in order to exclude particles that are only marginally or not uniquely bound to the system, e.g., lying in the protostellar envelope or flowing between the primary and secondary. The value was chosen empirically to be as small as possible while minimizing noise in the results.

To put this into practice, we use the SKID (Stadel 2001) group finder. SKID works by pushing tracer particles along density gradients to find local maxima, and linking them with friends of friends. Once group assignments are found, we remove unbound particles to create self-bound groups, computing

$$E = \frac{m_\mathrm{p}}{2}|\boldsymbol{v} - \boldsymbol{v}_\mathrm{cm}|^2 + U + E_\mathrm{th} \qquad (2)$$

as the total energy, with $\boldsymbol{v}$ and $\boldsymbol{v}_\mathrm{cm}$ the velocity and centre of mass velocity, U the gravitational potential and E_th the thermal energy. The centre of mass frame is updated throughout the unbinding procedure.

3 RUN A: RESULTS

At $t = 0.88\,t_\mathrm{ff}$, a nascent protostellar system has begun to form from the collapse of its enveloping core. In Fig. 1, the surface density and velocity field, projected through a $(1000\,\mathrm{au})^3$ box cut around the pre-stellar object, are shown. The box contains $0.29\,\mathrm{M}_\odot$ of gas. The central pre-stellar object formed via fragmentation of a filament 1000 au in extent. We see in the integrated transverse velocity field that accretion primarily occurs along the filament, as there is only a small torus of opening angles around the system from which low-density material is observed to make a direct approach. Most gas collides with the filament and is subsequently funnelled on to the system.

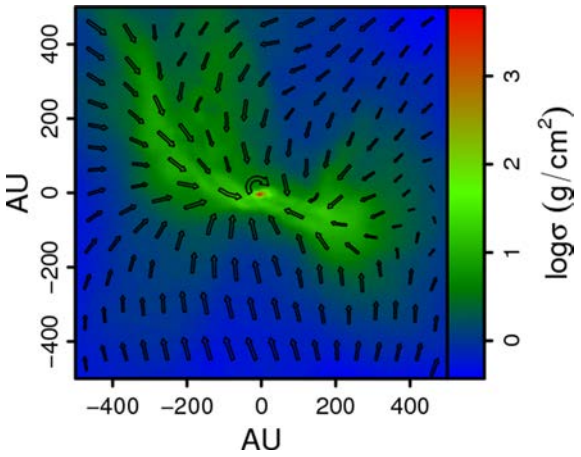

Figure 1. The column density and velocity field in a $(1000\,\mathrm{au})^3$ volume, containing $0.29\,\mathrm{M}_\odot$ of gas, around the central pre-stellar object. The time is $t = 0.88\,t_\mathrm{ff}$, the onset of core collapse.

In Fig. 2, the surface density of the pre-stellar system, in projection along its axis of rotation, is shown. The system is $0.055\,\mathrm{M}_\odot$ and the disc is 25 au. The filaments feeding the disc at this stage have densities ranging from $7 \times 10^{-15}\,\mathrm{g\,cm^{-3}}$ up to the critical adiabatic density $10^{-13}\,\mathrm{g\,cm^{-3}}$. The system accretes rapidly until $t = 0.893\,t_\mathrm{ff}$, whereupon a fragment of mass $8 \times 10^{-3}\,\mathrm{M}_\odot$ forms in the low-density filamentary material, close to the Jeans mass of $6.4 \times 10^{-3}\,\mathrm{M}_\odot$. The fragment survives first pericentre and becomes a companion. The isolated system, in contrast, continued accreting material rapidly, building up the disc around the protostellar system.

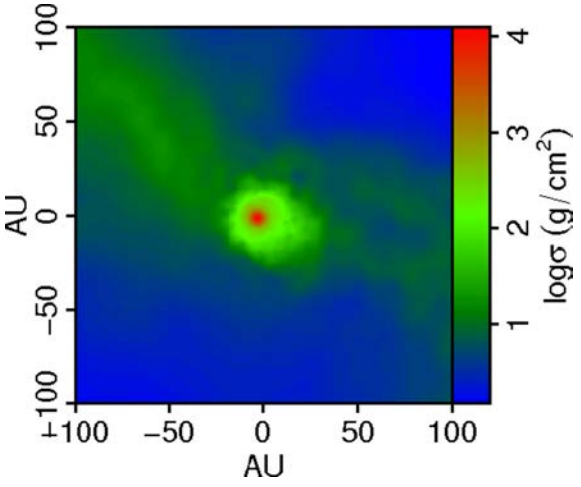

Figure 2. The protostellar object formed at the onset of its parental core's collapse at $t = 0.88\,t_\mathrm{ff}$. The object is 1.7 kyr old at this stage with a disc of 25 au in radius and a mass of $0.055\,\mathrm{M}_\odot$.

3.1 Surface densities and temperatures

3.1.1 Surface density maps

In this section, we compare the divergent evolution of the isolated and binary systems. To accommodate the change in dynamical times at disc scales, we set the units to kyr and count time relative to the formation of the system at $0.88\,t_{\rm ff}$. In Fig. 3, we see the surface density maps of the isolated and the binary systems in the left- and right-hand columns, respectively, shown at times 4.4, 5.8 and 7.1 kyr after the formation of the primary (or equivalently, the

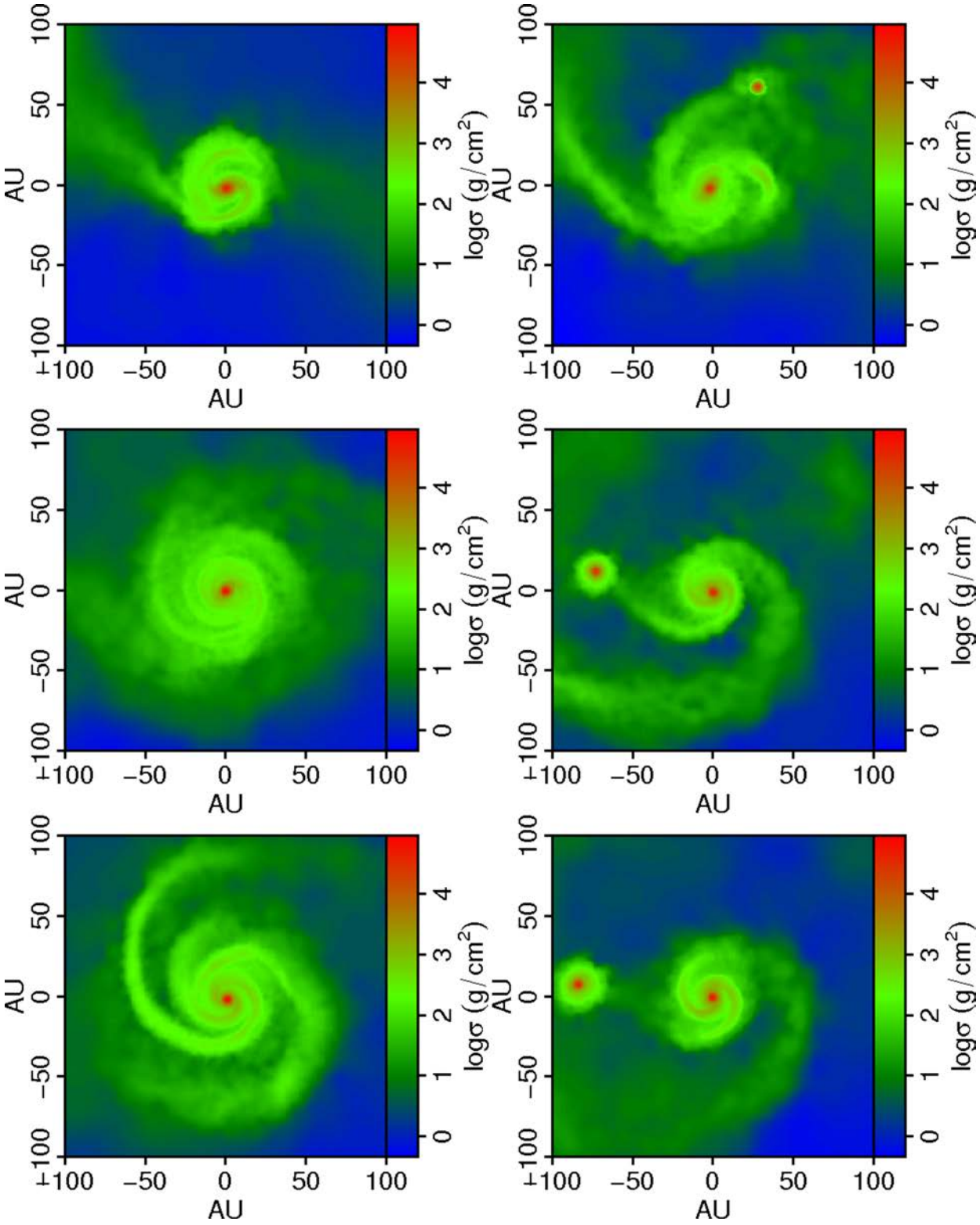

Figure 3. The surface densities of the isolated and binary systems, respectively, in the left- and right-hand columns, and shown at times 4.4, 5.8 and 7.1 kyr from the top row to bottom, after formation.

isolated system). Differences appear early between the two systems. In the topmost row, we see that the primary in the binary system is similar to the isolated system in morphology and surface density except for a tidal disturbance of the disc caused by an initial close passage of the secondary. In the central row, the differences are more pronounced. At 5.8 kyr, we see that the isolated system has continued to grow in mass, and the disc now has a radius of 50 au. Between 4.4 and 5.8 kyr, approximately one orbital time has passed in the binary system, and the secondary is at its apogee. The primary has shrunk in extent as the secondary has accreted some gas from its outer regions. The secondary is also rapidly accreting high specific angular momentum gas from the two filaments feeding the system. In the bottom row at 7.1 kyr, we see that the isolated system has continued to grow in mass and extent but has become gravitationally unstable, and an $m = 2$ spiral arm has developed into a material arm. At 7.1 kyr, the binary system has completed another orbit, both systems have grown in mass, and the same pattern of tidal disturbance of the primary is observed.

3.1.2 Temperature maps

In Fig. 4, mass-weighted temperature maps of the binary and isolated systems, at times 4.4, 5.8 and 7.1 kyr, are plotted, as in Fig. 3. As we are using a piecewise polytropic EOS (equation 1), some of the gas bound at the outer edge of the system(s) and some interarm gas is still in the isothermal phase. In the isolated system, increasing amounts of mass end up at large radii and at low densities due to its higher specific angular momentum j (see Section 3.2 for elaboration on these points). In the binary system, however, pictured in the right-hand column of Fig. 4, almost all of the mass identified as bound to each system lies at high densities (and is thus adiabatic) and within their respective tidal radii.

3.2 Disc evolution

3.2.1 Disc mass

In Fig. 5, the accretion histories of the isolated, primary and secondary systems are plotted. The mass at a given time is determined by the procedure outlined in Section 2.4 and is thus the combined protostellar and disc mass. The isolated system accretes gas steadily and at a high rate throughout the simulation, with typical accretion rates of 3×10^{-5} to $5 \times 10^{-5}\,\mathrm{M}_\odot\,\mathrm{yr}^{-1}$. After the initial collapse, the central protostar, defined as the mass contained within $r < 5\,\mathrm{au} \simeq 2\epsilon$, has an accretion rate of 5×10^{-6} to $6 \times 10^{-6}\,\mathrm{M}_\odot\,\mathrm{yr}^{-1}$. Taking the asymptotic rate from 1D protostellar collapse theory, $\dot{M} = m_\circ c_\mathrm{s}^3/G$ (Stahler & Palla 2005), we find that $\dot{M} = 2 \times 10^{-6}\,\mathrm{M}_\odot\,\mathrm{yr}^{-1}$, and so $m_\circ$, a constant of the order of unity, is approximately 2.5 at the protostar. This is not a high accretion rate, as 1D collapse simulations asymptote to $m_\circ = 2$ (Stahler & Palla 2005). The accretion rate on to the entire system, however, is high, with $m_\circ \sim 10$, and is perhaps due to embedding within a filament. Both accretion rates are consistent with other studies, such as those found in Walch et al. 2010.

As expected, the net mass accreted by the binary system is close to that of the isolated one. The difference between the two is because there is some mass present in the binary that cannot be uniquely assigned either to the primary or the secondary. The binary system is plotted starting at 3.8 kyr, instead of its formation time at 3330 years, because during the first pericentre the identification procedure has difficulties separating the two objects uniquely. In the binary system, the secondary, due to its orbit, preferentially accretes high specific angular momentum gas from the filaments and accretes mass at a higher rate than the primary, and at later times the mass ratio tends towards unity. This behaviour has been noted before in the literature (e.g. Bate & Bonnell 1997).

In Fig. 6, the ratio of stellar mass (the mass within 5 au, chosen to correspond with the limits of our softening) to disc mass for the isolated and primary systems are plotted. The isolated system continues gaining disc mass faster than it can be transported to the star, while the primary evolves steadily towards stability. As systems normally become moderately self-gravitating at a mass ratio of $\sim$0.1, we see that these newly formed protostellar systems are in a regime dominated by gravitational instability.

3.2.2 Cumulative mass fraction and mass profiles

The discs in both the isolated and binary systems are all massive relative to the central protostar and exhibit strong spiral arms as seen in Fig. 3. We expect that tidal torques will, in addition, play a role in triggering mass transport within the discs in the binary as noted, for example, in Mayer et al. (2005). In Figs 7 and 8 are plotted the surface densities averaged in annuli of the isolated disc and of the primary of the binary system. We see from Fig. 7 that in the isolated system, the trend as time progresses is towards increasing amounts of mass at all radii, while from Fig. 9 it is evident that the relative amount of mass at large radii is increasing, illustrated by the outward movement of the half-mass radius. The surface density profile of the primary in the binary system (see Fig. 8) shows increasing surface density within 20 au and clearly decreasing surface density outside of 30 au throughout the simulation. This is reflected in the cumulative mass profile in Fig. 10 as a decreasing overall fraction of mass found at larger radii and the clear inward movement of the half-mass radius (while the total mass slowly increases). The source of this difference is likely increased mass transport from gravitationally amplified tidal perturbations. To illustrate the role of tidal effects, we model the primary and secondary as point masses and compute the Jacobi radius r_j at 5.8 kyr given the nominal values $M = 0.125\,\mathrm{M}_\odot$, $m = 0.05\,\mathrm{M}_\odot$ and $R_0 = 75$ au (see Figs 5 and 3) for the primary mass, secondary mass and separation, respectively. Given these parameters, we compute $r_\mathrm{j} = 0.41R_0 = 31$ au; thus, we expect tidal effects to, at the very least, limit the disc of the primary to 44 au. Looking at the cumulative mass profile, we see that our disc-finding procedure is roughly consistent with such a simple model, with very little bound mass found outside of 30 au.

3.2.3 Temperature profiles

In Figs 11 and 12 are plotted the temperature profiles in the isolated and binary systems, respectively. At times 4.4 and 5.8 kyr, the temperature declines steadily from 250 to 10 K at 40 and $\sim$60 au, respectively, whereupon it remains at the temperature floor for larger radii; however, there is little mass at these radii (see Fig. 9). At time 7.1 kyr, the disc becomes more extended, and the temperature profile flattens at large radii. The disc contains a mixture of isothermal and adiabatic gas, with the spiral arms containing most of the adiabatic component. In the binary system (Fig. 12), the temperature profiles of the primary lack the low-temperature, low-density component seen in the isolated system due to truncation of the disc at the tidal radius and do not evolve much after 5.8 kyr.

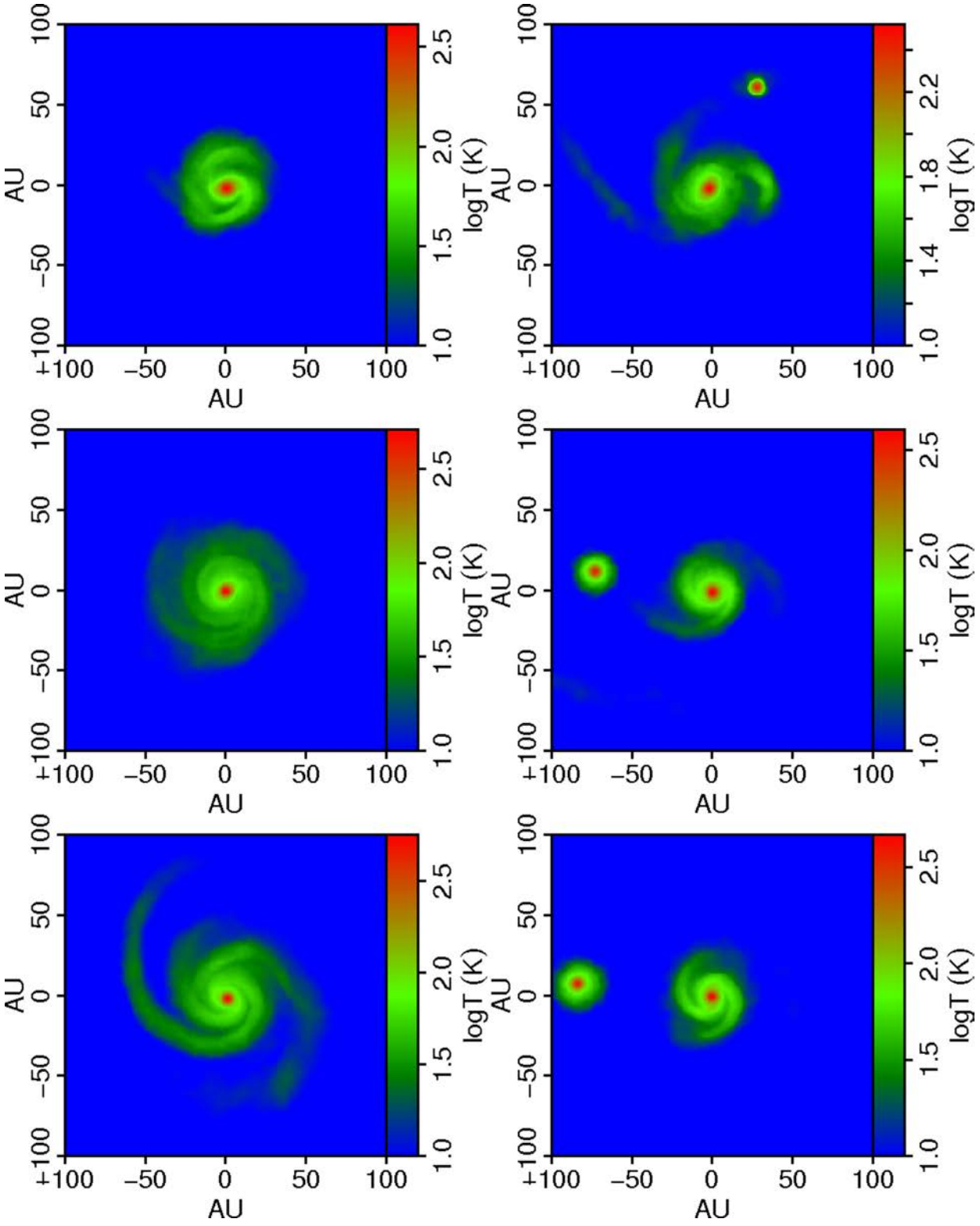

Figure 4. Mass-weighted temperature maps of the isolated and binary systems, respectively, in the left- and right-hand columns, and shown at times 4.4, 5.8 and 7.1 kyr from the top row to bottom, after formation.

3.2.4 Specific angular momentum

In Fig. 13 are plotted the combined disc and protostellar specific angular momenta for the isolated, primary and secondary systems. Each measure is computed in the centre of mass frame of the given systems and is thus a measure of the spin (i.e. disc) component of the specific angular momentum. The isolated system rapidly increases in specific angular momentum, and after 7.1 kyr, becomes unstable to fragmentation. In the binary system, the primary has a small spike in its specific angular momentum j at 4.2 kyr due to weakly bound

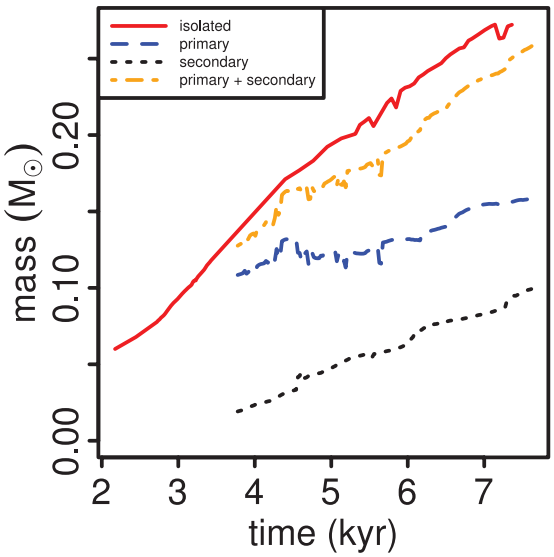

Figure 5. Total mass accreted (disc + protostar) versus time for the isolated, primary and secondary systems, and the net mass in the binary system.

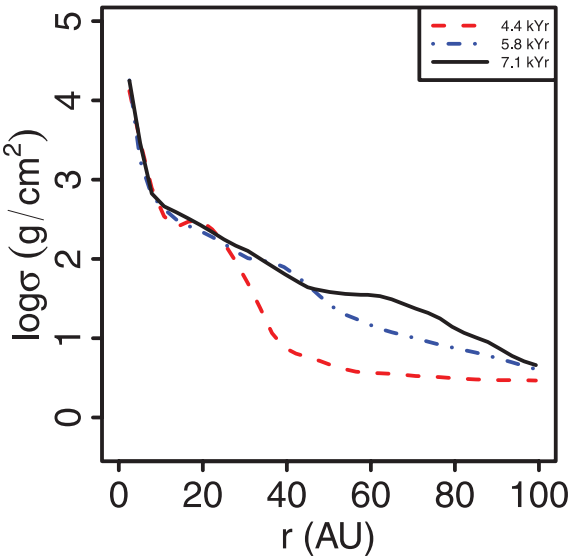

Figure 7. Evolution of the surface density profile of the isolated system. σ tends to increase at all radii with time.

material appearing to be bound to the primary, while the secondary reaches pericentre. This is also seen in the mass plot at the same time. The primary exhibits very little evolution in j thereafter, while from Fig. 5 we see that it continues to accrete mass in the interim; it accretes at constant j. In contrast, the secondary increases steadily in j along with M.

Part of the reason that the binary increases more slowly in specific angular momentum than the isolated system is that it is able to store momentum in the binary orbit. To measure this effect, we use the relationship

$$\boldsymbol{L} = \sum_i \boldsymbol{R}_i \times \boldsymbol{P}_i = \boldsymbol{R} \times \boldsymbol{P} + \sum_i \boldsymbol{r}_i \times \boldsymbol{p}_i, \quad (3)$$

where $\boldsymbol{L}$ is the angular momentum, $\boldsymbol{R}_i$ are the positions of each particle, $\boldsymbol{P}_i$ are the particle momenta, $\boldsymbol{R}$ is the barycentre, $\boldsymbol{P}$ the velocity of the barycentre, $\boldsymbol{r}_i$ and $\boldsymbol{p}_i$ the positions and momenta relative to the barycentric frame, and decompose the binary into spin and centre of mass angular momenta. We further get the specific angular momenta using the appropriate mass weightings along with equation (3). At $t = 7.1$ kyr, we find that in the barycentric frame, the isolated system has a specific angular momentum of 7.0×10^{19} cm^2 s^{-1}. In the binary system, the binary orbit itself has 6.1×10^{19} cm^2 s^{-1}, the primary has 3.0×10^{19} cm^2 s^{-1} and the secondary has 1.3×10^{19} cm^2 s^{-1} (also visible from Fig. 13). The specific angular momentum of the binary orbit dominates that found in the other components.

We quantify alignment of the specific angular momentum of the disc with that of the environment by computing the angle $\theta = \cos^{-1}(\hat{\boldsymbol{j}}_\mathrm{d} \cdot \hat{\boldsymbol{j}}_\mathrm{e})$, with $\hat{\boldsymbol{j}}_\mathrm{d}$ being the unit vector of the specific angular momentum of the disc and $\hat{\boldsymbol{j}}_\mathrm{e}$ being that of the material in the

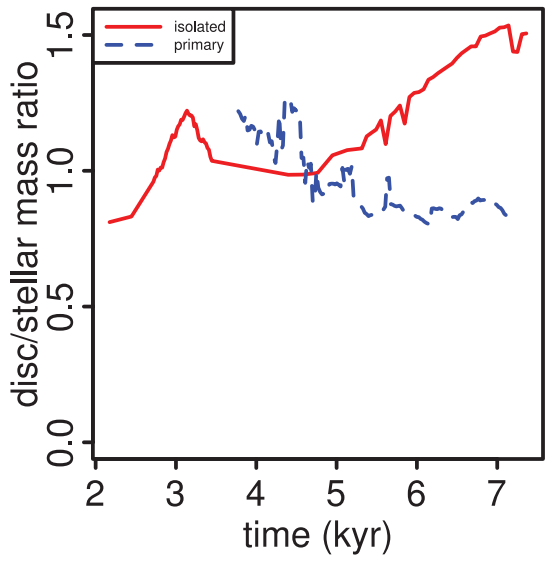

Figure 6. The ratio of disc mass to accreted stellar mass versus time, for the isolated and primary systems.

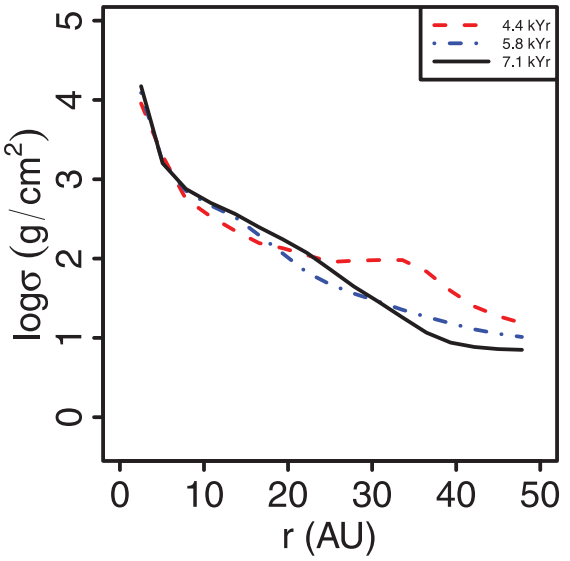

Figure 8. Evolution of the surface density profile of the primary in the binary system. σ decreases steadily at outer radii and increases at inner radii due to tidal interactions.

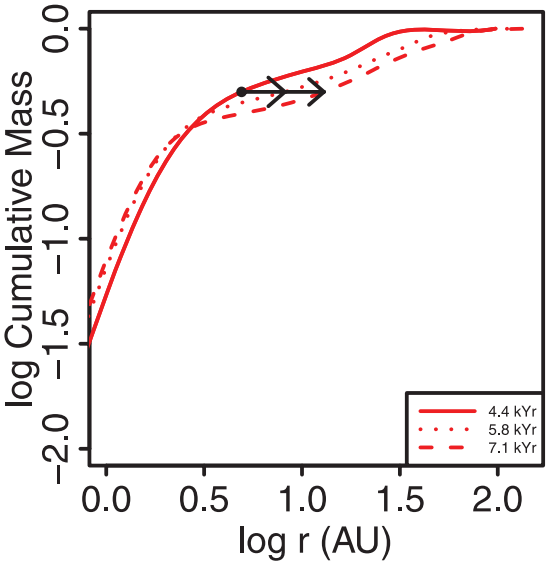

Figure 9. The mass profile evolution of the isolated system. As time progresses, increasing amounts of mass relative to the total lie at large radii. We illustrate this by plotting the evolution of the half-mass radius in black.

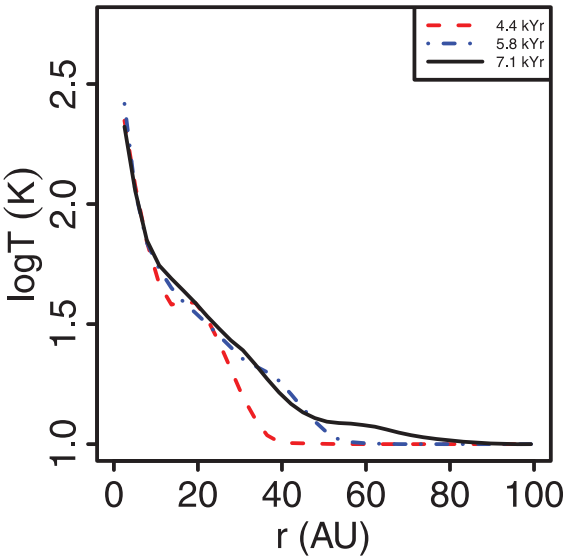

Figure 11. Azimuthally mass-averaged temperatures in the isolated system. At later times, the high j gas has formed an extended disc which includes cold interarm gas around the primary, leading to a break in the temperature profile.

environment in a box of dimensions 2000^3 au^3 surrounding the system. At the time of formation of the system (Figs 1 and 2), we find $\theta = 36^\circ$. In the isolated system, we observe angles of 13°, 7.°7, 12° at times 4.4, 5.8 and 7.1 kyr, respectively. In the binary system, the $\hat{\mathbf{j}}_{\rm d}$ of the primary is 18°, 7.°3, 5.°3 at times 4.4, 5.8 and 7.1 kyr. The vectors tend to be oriented perpendicular to the major axes of the filaments feeding the disc. Such relatively small misalignments are consistent with other works suggesting filaments tumbling about one of their shorter axes as the origin of protostellar angular momentum (Walch et al. 2010) and with observations of protostellar systems on these length-scales, which find that most gas is extended in the direction perpendicular to outflows (Tobin et al. 2010).

3.3 Stability and fragmentation

Throughout the simulation(s), the discs of both the isolated and binary systems are massive and gravitationally unstable. To compare stability, we compute the Toomre $Q = c_{\rm s}\kappa/\pi G\sigma$ parameter locally using mass-weighted projections, through a $200 \times 200 \times 200$ au^3 box, followed by azimuthal averages, of the disc. The results are shown in Figs 14 and 15. Although the Q curve for the isolated system drops below unity in some regions at 4.4 kyr, it does not fragment right away. As the envelope is accreted, the disc evolves to a state where Q lies between 1 and 2 out to 90 au. The disc remains in the unstable regime, but Q varies substantially as the system accretes. In contrast, the primary of the binary system has a minimum Q of 1.3 at later times and, except initially, rises above 2

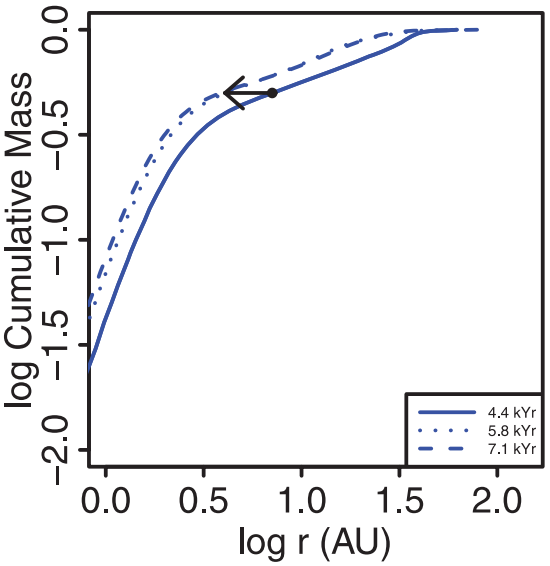

Figure 10. The mass profile evolution of the primary. In contrast to Fig. 9, we see the relative fraction of mass at large radii decreasing with time. We illustrate this by plotting the evolution of the half-mass radius in black.

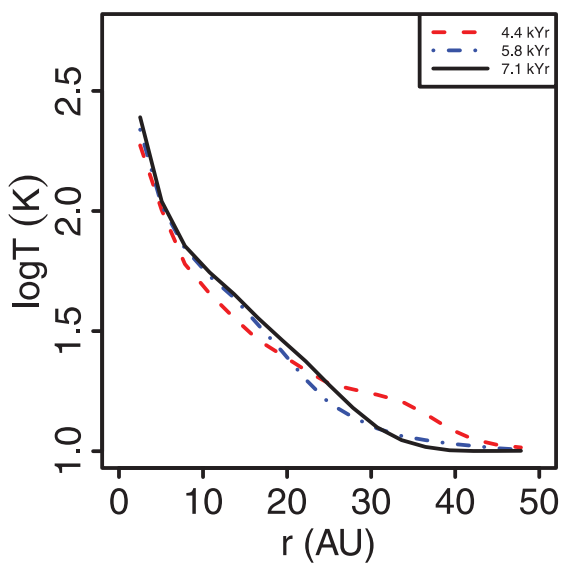

Figure 12. Azimuthally mass-averaged temperatures in the primary of the binary system. The disc remains limited by tidal forces, and almost all bound gas is adiabatic.

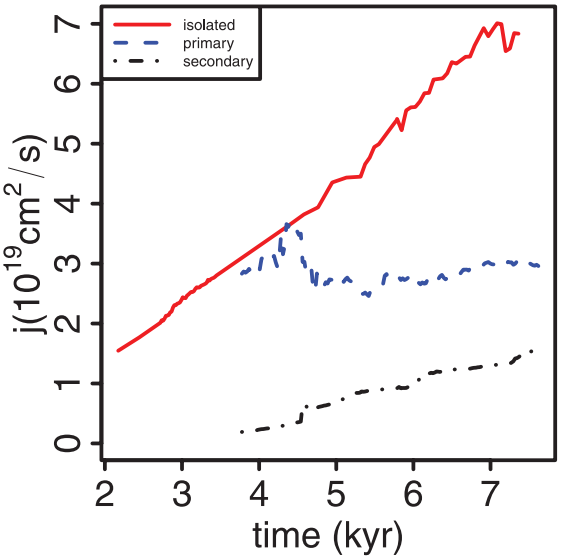

Figure 13. Evolution of the specific angular momentum j of the isolated and binary systems. j grows rapidly for the isolated system and leads to a more rapid build-up of an extended disc, whereas tidal effects and lower j lead to smaller discs in the binary system.

at radii greater than 25 au. The binary system is thus significantly more stable than the isolated one, and this is borne out by the fact that it does not fragment at later times (up to 20 kyr).

At 9.2 kyr, we find that the isolated system becomes unstable to fragmentation, forming two clumps, one at $r = 65$ au, followed by another at $r = 100$ au in the disc. The first clump (C1) formed in one of the material arms of the disc from adiabatic gas, with an initial mass of 5.5 $M_{\rm jup}$ and specific angular momentum of 1.8×10^{18} cm^2 s^{-1}. The second clump (C2) formed at 10 kyr had a mass of 7.4 $M_{\rm jup}$ and specific angular momentum of 3.2×10^{18} cm^2 s^{-1}. We seek to understand the formation of the first clump from adiabatic gas by looking at the behaviour of Q in the run-up to fragmentation. In Fig. 16 is plotted the Q parameter averaged in an annulus ranging from 60 to 70 au. Q starts off initially very high but drops as

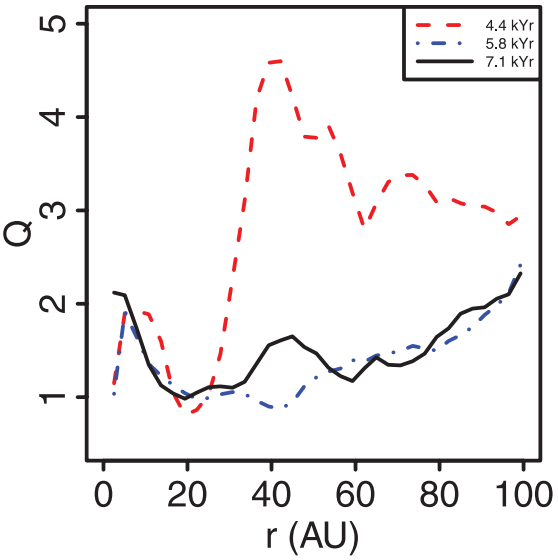

Figure 14. Azimuthally averaged Toomre Q for the isolated system at times 4.4, 5.8 and 7.1 kyr.

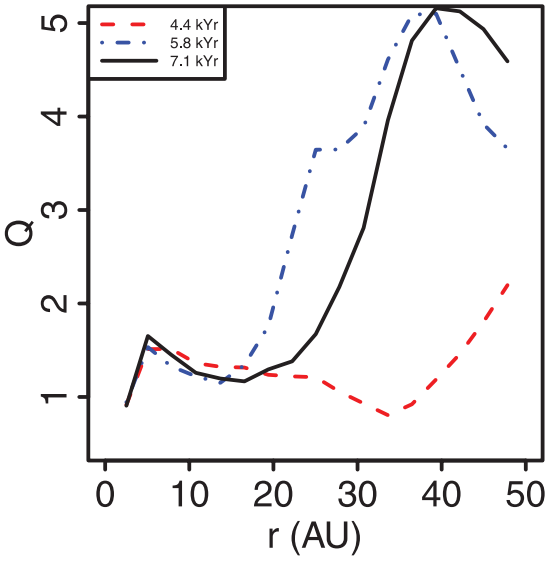

Figure 15. Azimuthally averaged Toomre Q for the binary system at times 4.4, 5.8 and 7.1 kyr. The binary system remains stable for as long as the simulation was run (20 kyr).

continuing accretion builds up the disc in this region. Both clumps are depicted in Fig. 17 at 11 kyr. At this time, clump C1 has made approximately 1.5 orbits and has a mass of 39 $M_{\rm jup}$, and clump C2 one half-orbit and has grown to 14 $M_{\rm jup}$. Both clumps accrete at a rate of roughly 10^{-5} M$_\odot$ yr^{-1}.

4 RUN B: RESULTS

We describe here the results from a complimentary simulation, run B. At approximately $t = 1.1\,t_{\rm ff}$, fragments form at either end of a long (7400 au) filament, within ∼2 kyr of each other. In the following discussion and figures, we set $t = 1.1\,t_{\rm ff}$ as being $t = 0$, as it is at this time when the first system, the isolated system, forms.

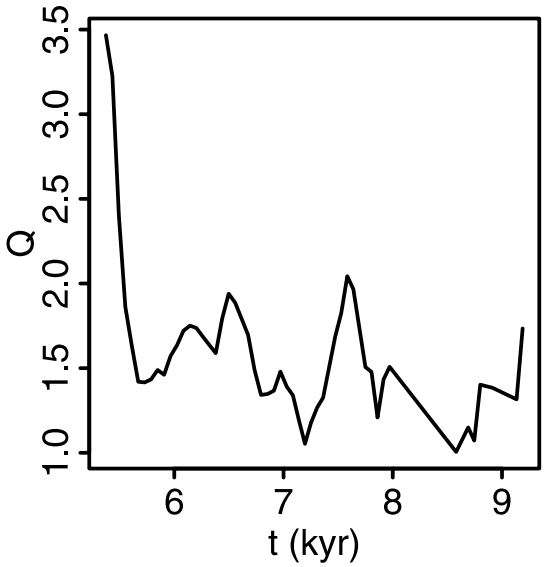

Figure 16. Toomre Q paramater of the isolated system averaged in an annulus from 60 to 70 au in times preceding clump formation. A clump later forms at 9.2 kyr at 65 au.

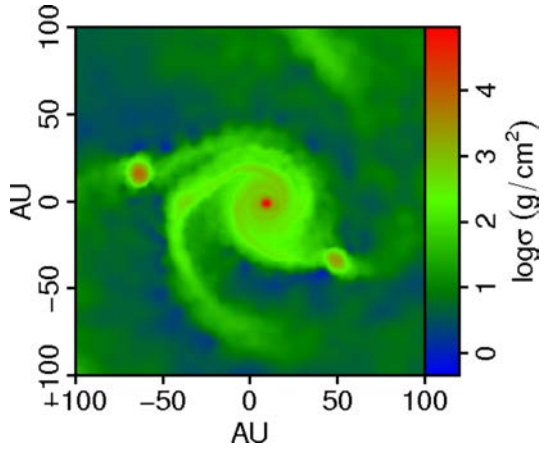

Figure 17. A surface density map of the isolated system at $t = 11$ kyr, approximately one orbital time after the second fragment formed.

The upper left-hand image in Fig. 18 is a surface density plot of the filament projected through a $(10^4\,\mathrm{au})^3$ box. At the top end of the filament lies the isolated system, and the cluster is located at the bottom. The upper right-hand image in Fig. 18 is the surface density of the cluster at the end of simulation. Only three of the four members are shown. The two systems in the upper left-hand corner of the image have formed a binary, in the sense that they complete orbits around their centre of mass on a time-scale shorter than the cluster crossing time. For a more complete discussion of the cluster evolution, see Section 4.1.

In the second and third rows of Fig. 18 are the surface densities and mass-weighted temperature maps of the isolated system (lying at the top of the filament) at 4.3 and 8.7 kyr. In the isolated system, we see the disc assemble rapidly from infalling filamentary gas, going through stages of increasing gravitational instability until, as shown in the bottom row of Fig. 18, the gas trailing at the end of one of the material arms in the disc fragments. As seen in the temperature maps, the gas in the fragment was in the adiabatic regime. The initial clump mass is $12\,M_{\mathrm{jup}}$.

4.1 Cluster evolution

In Fig. 19 are plotted the distances of cluster members to the origin of a fiducial cluster frame versus time. Since the cluster is a rapidly evolving object at this stage, we choose the fiducial frame as being the one which moves in a straight line from the original position of the first clump to its final position. We can see in Fig. 19 that members are typically $\sim$100 au from the origin in this frame. Members spend most of their time in binary associations, whereby it is meant that they orbit around their common centre of mass on time-scales shorter than the cluster crossing time. Two such binaries can be seen at points A and B in Fig. 19 through the mutual oscillation of their distances in the cluster frame. At point C in the figure, the members of the cluster converge briefly and their mutual separations become comparable to their binary separations. Between C and D, a merger occurs, and a new binary forms, with the remaining member being sent on a larger orbit.

4.2 Disc evolution

4.2.1 Disc mass

In Fig. 20, the accretion histories of the isolated system and those of all objects formed in the cluster are plotted. The isolated system accretes gas at a high rate at an average of $8 \times 10^{-5}\,\mathrm{M}_{\odot}\,\mathrm{yr}^{-1}$. The accretion rates observed are quite comparable to those for the isolated system from run A, and thus they are well above the expected asymptotic rates ($m_{\circ} \gtrsim 10$).

For the cluster, the average accretion rate is $\sim 3 \times 10^{-5}\,\mathrm{M}_{\odot}\,\mathrm{yr}^{-1}$, with little deviation between objects. The evolution of the cluster is complex. The pattern of fragmentation of core gas never yielded objects which were isolated for very long, quickly leading to the production of a couple of short-lived binaries with similar evolution (similar accretion rates and generally limited disc size). A major merger occurs at 6.3 kyr; the result of a head-on collision between two clumps. Given the chaos of the cluster, the accretion rates as seen by the slopes in Fig. 20 are remarkably uniform.

4.2.2 Specific angular momentum

In Fig. 21 are plotted the combined disc and protostellar specific angular momenta for the isolated system and for the objects in the cluster. As in run A, the isolated system rapidly increases in specific angular momentum. Upon reaching $\sim 7 \times 10^{19}\,\mathrm{cm}^2\,\mathrm{s}^{-1}$, material arms form in the isolated system, moving angular momentum out of the system and allowing angular momentum to remain constant while accretion continues (cf. Fig. 20). As the arms become stronger, the determination of j becomes more difficult, because gas is ejected with increasing violence from the ends of the material arms back into the envelope. About 1 kyr after the onset of this behaviour, the arm fragments (shown in Fig. 18).

The evolution of the cluster angular momenta shows a rather remarkable contrast. Following Fig. 21 once more, we see that the first object to form in the cluster evolves as one might expect, with both mass and specific angular momentum increasing. Once other fragments form in the cluster, the specific angular momentum of the system drops until hitting a maximum value which appears to characterize the entire cluster. The pattern of fragmentation in the core never left any object in the cluster truly isolated for very long, with some short-lived binaries forming, sometimes ending in mergers, but generally lasting long enough to tidally limit and alter the structure of the discs of cluster members. Referring once more to the mass evolution plots in Fig. 20, we see that accretion continues, somewhat abated by the competition amongst cluster members for infalling gas. We see then a stronger, clearer, reiteration of the result from run A, namely that upon hitting a threshold, accretion continues but at a constant specific angular momentum.

The major merger occurring at 6.3 kyr, indicated by the large filled circles in Fig. 21, has an interesting effect on the angular momenta of the merging systems. Their momenta both dip quite suddenly at the time of collision. This is due to the ejection of plumes of high-j gas at the moment of merger. The gas is then quickly accreted on to the new system, bringing it back up to the angular momentum ceiling for the cluster.

5 DISCUSSION

5.1 Fragmentation

5.1.1 Accretion and specific angular momentum

In the simulations performed, the isolated systems become prone to fragmentation via the development of massive material arms, even though the gas is adiabatic. Instabilities in the isolated systems are driven by steady accretion of gas with increasing specific angular momentum. The disc, sufficiently massive to generate spiral arms,

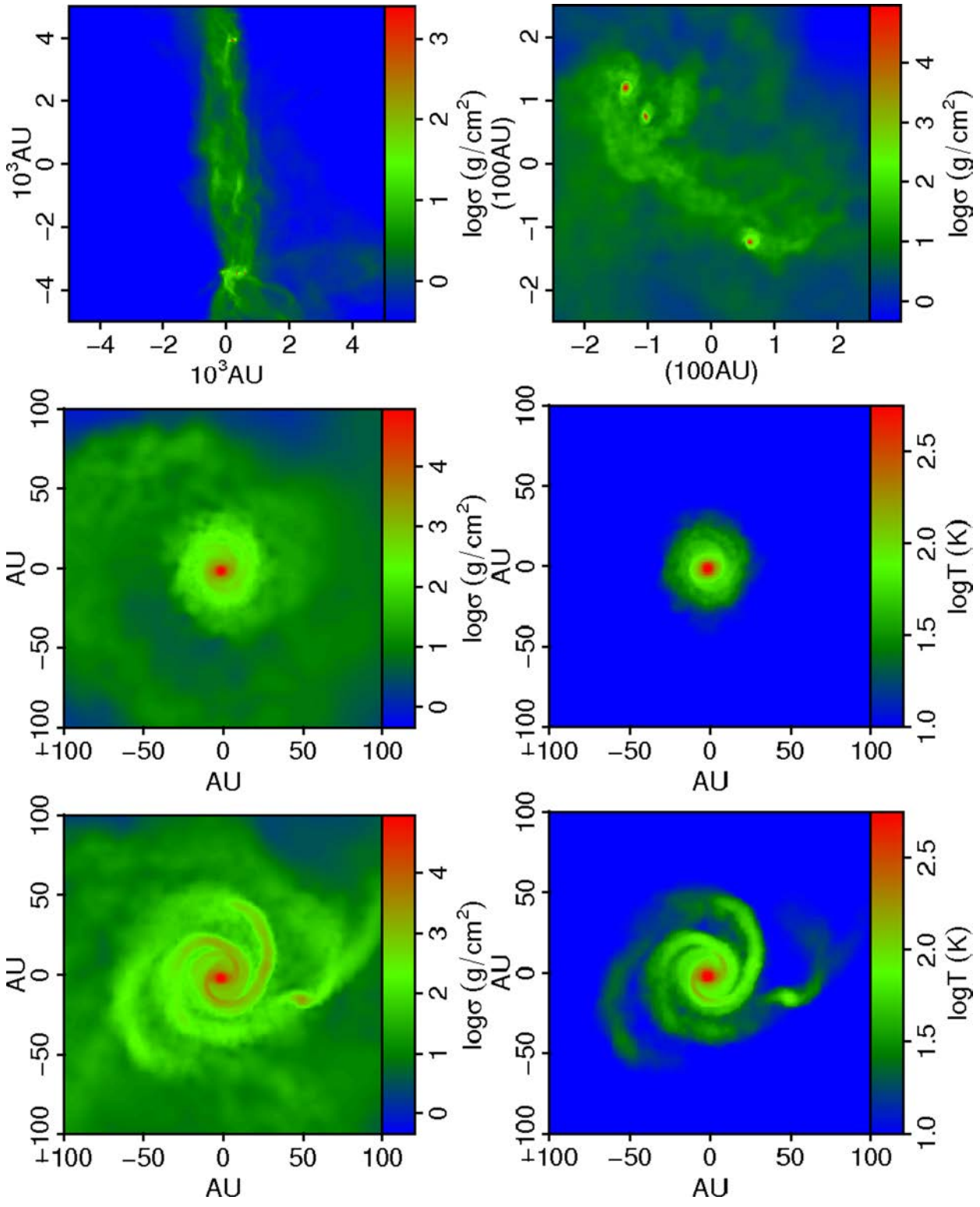

Figure 18. First row, left: surface density map of filament formed in run B. At the top and bottom of the filament are the isolated system and cluster, respectively. Right: the cluster as seen at the end of the simulation. One member, 10^3 au away, is not shown. Second and third rows: the surface densities and mass-weighted temperature maps of the isolated system, respectively, in the left- and right-hand columns shown at times 4.3 and 8.7 kyr after formation.

accumulates a reservoir of gas lying at large radii (i.e. with high specific angular momentum). This reservoir is then swept up by the spiral arms, which, when sufficiently massive, become prone to fragmentation; such instabilities have been documented in similar contexts in the literature (e.g. Bonnell 1994; Whitworth et al. 1995; Hennebelle et al. 2004). At the same time, Offner et al. (2008) observe that in simulations of freely decaying turbulence, the resulting protostellar systems are more prone to fragmentation, and

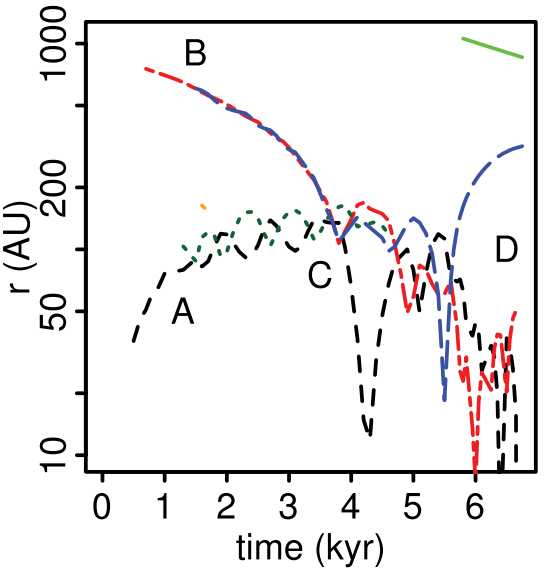

Figure 19. Distance from the origin of a fiducial cluster frame of reference versus time for various members of the cluster. The frame of reference is based on the trajectory of the oldest member; hence, the separation approaches zero at the beginning and end of the data. Several objects pair up to form short-lived 'binaries' while in the cluster. Two such binaries can be seen at points A and B in Fig. 19 through the mutual oscillation of their distances in the cluster frame. At point C, all extant members of the cluster briefly converge. Between C and D, a merger occurs, leading to the formation of a new binary and the ejection of the third member.

attribute it to high rates of accretion. Seeing as all systems in the present study have accretion rates several times that of the nominal 1D asymptotic rate, perhaps the tendency towards fragmentation observed by Offner et al. (2008) is due to a combination of higher accretion rates *and* accretion of gas with high specific momentum. Furthermore, it could be that the continued driving of turbulence is reducing the specific angular momentum of accreted gas, or acting as a viscosity and depleting the reservoirs of gas which would otherwise be swept up in dense material arms.

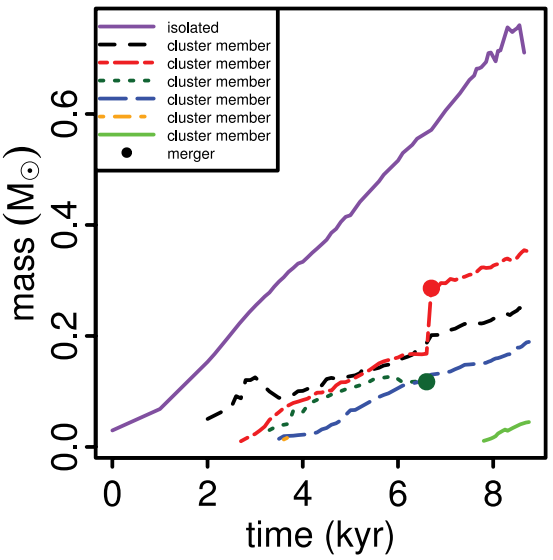

Figure 20. Total mass accreted (disc + protostar) versus time for the isolated system, and the cluster. A merger occurs between two pre-stellar systems in the cluster at 6.3 kyr.

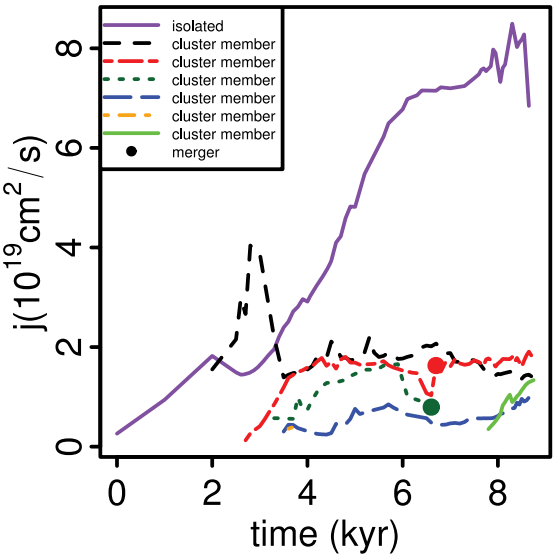

Figure 21. Evolution of the specific angular momentum j of the isolated system and the cluster. j grows rapidly for the isolated system and leads to a more rapid build-up of an extended disc, whereas various tidal effects and close encounters lower j and lead to smaller discs in the binary system.

The binary system from run A and the systems in the cluster from run B remain stable throughout the simulation. Although the discs are sufficiently massive to be self-gravitating and the systems are accreting, a number of effects work against outer disc fragmentation. The tidal limiting of the discs, as discussed in Section 3.2.2, is a major barrier to fragmentation. In run A, although the binary separation evolves (increases) throughout the simulation, by the end of our run the separation is ∼75 au, and given the tendency of the binary mass ratio to approach unity (e.g. Bate & Bonnell 1997), there is very little chance for outer disc fragmentation to occur. In run B, the cluster appeared to have an effective ceiling in the specific angular momentum for member systems. Longer simulations looking at the long-term evolution of multiple systems and clusters should be undertaken to see if they separate sufficiently to allow extended discs to grow. Even if at some later point they do grow, fragmentation is less likely because most mass will likely have made it on to the star and a high disc/star mass ratio will be harder to achieve; also, accretion rates decrease as time progresses. In run A, the tendency for the secondary to accrete high specific angular momentum gas, as seen in this paper and in other studies of binaries (e.g. Bate & Bonnell 1997), acts strongly to deplete the reservoir of gas in the outer part of the system and shuts out the possibility for the growth of the same Toomre instability which led to fragmentation of the isolated system. Furthermore, the enhanced inward transport of mass due to tidal torques shown in Section 3.2.2 acts to stabilize the disc against fragmentation, an effect that has also been observed by e.g. Mayer et al. (2005).

5.1.2 Accretion and gas temperatures

In the following, we discuss and analyse run A in more detail. In the isolated system, two clumps form by the end of the simulation. They form in the outer reaches of the disc where temperatures were low, and where some interarm gas is still isothermal at 10 K, although clump C1 forms in a material arm from adiabatic gas with a temperature of ∼30 K. Recent simulations of star formation including a flux-limited diffusion treatment for radiative transfer and

some modelling of protostellar accretion emphasize the importance of radiative feedback on the envelope. To estimate the effect, we compute the accretion luminosity of the protostar (Stahler & Palla 2005):

$$L_{\rm acc} = \frac{GM_\star \dot{M}}{R_\star} = 61\,{\rm L}_\odot \left(\frac{\dot{M}}{10^{-5}\,{\rm M}_\odot\,{\rm yr}^{-1}}\right)\left(\frac{M_\star}{1\,{\rm M}_\odot}\right)\left(\frac{R_\star}{5\,{\rm R}_\odot}\right)^{-1}, \quad (4)$$

with $M_\star = 0.11\,{\rm M}_\odot$ being the protostellar mass, which we compute by taking all mass within $r \leq 5\,{\rm au} \simeq 2\epsilon$; $\dot{M} = 5 \times 10^{-6}\,{\rm M}_\odot\,{\rm yr}^{-1}$ is the (time-averaged) accretion rate on to the protostar and $R_\star$ is the protostellar radius that, since it is subgrid, we assume has a fiducial value of $5\,{\rm R}_\odot$. From this, we get a typical accretion luminosity of $L_{\rm acc} = 3.4\,{\rm L}_\odot$. Clump C1 forms at $r_{\rm c} = 65\,{\rm au}$. To try to get an upper limit on the temperature at that radius, we assume that the disc presents an absorbing surface of height $h = 10\,{\rm au}$ spanning $r_{\rm c} \pm 5\,{\rm au}$ and that all of the accretion luminosity crossing this surface deposits all of its energy in this region, yielding a heating rate of $L_{\rm acc}h/2r_{\rm c} = 10^{33}\,{\rm erg\,s^{-1}}$. We assume D'Alessio, Calvet & Hartmann (2001) opacities and a 1-μm grain size, and a background irradiation temperature of 30 K, and using the existing density field of the gas within $r_{\rm c} \pm 5\,{\rm au}$ at the time of fragmentation, we calculate the temperature at which the cooling rate balances the heating rate of the gas to be 50 K. We wish to emphasize that the assumptions made here are extremely conservative with the aim of bracketing the upper end of conceivable outer disc temperatures. Given the weak dependence of Q on T, it does not appear that the accretion luminosity will be able to affect the disc stability at these large radii.

5.1.3 *Clump masses and accretion rates*

Again, we limit the discussion here to run A for brevity. The isolated system forms two clumps of masses 5.5 and $7.4\,M_{\rm jup}$. What kind of clump masses should one expect in the outer disc? Because the disc is in a disordered state at the time of clump formation, we do not compare the clump masses to those computed from axisymmetric models, but instead we compute the local Jeans mass of the clump-forming gas, which for clump C1 was $4.7\,M_{\rm jup}$, and that of clump C2 was $4.5\,M_{\rm jup}$. The particle mass in the simulations was $10^{-5}\,{\rm M}_\odot$; hence, in the clumps the Jeans mass is resolved with ∼450 particles, or ∼14 smoothing kernels. The fragmentation phenomena are thus well resolved according to the criteria set forth in the literature (Bate & Burkert 1997; Nelson 2006). In addition, the initial angular momentum radii of the clumps are 0.31 and 0.73 au, respectively, and should they undergo a second collapse in $\sim 10^4$ years due to H_2 dissociation, any accretion on to the final body will take place through an accretion disc (Boley et al. 2010). We observe final clump masses of 3.9 and $14\,M_{\rm jup}$ for C1 and C2, respectively; however, whether or not dissociative collapse will occur before these masses are achieved is highly sensitive to assumptions about the dust. We emphasize here that the connection between our final obtained clumps and the substellar companions (the planets or brown dwarfs) produced from them is uncertain. A dissociating collapse of the clumps and the establishment of an accretion disc are a certainty; however, other dynamical instabilities may form, such as a bar instability, and can play a role in redistributing mass and angular momentum. Because the simulation lacks the necessary physics and resolution to follow the internal evolution of the clumps, we refrain from speculating on the final object masses. Nevertheless, we can estimate accretion luminosities for our final clumps using our clump parameters. Both clumps C1 and C2 had accretion rates of $\sim 10^{-5}\,{\rm M}_\odot\,{\rm yr}^{-1}$. Computing the accretion luminosity using equation (4), inputting the measured accretion rate, clump masses of 5.5–39 $\,{\rm M}_\odot$, and assuming a fiducial final size of $1\,R_{\rm jup} = 7 \times 10^9\,{\rm cm}$, give accretion luminosities ranging between 16 and $110\,{\rm L}_\odot$. Such relatively high luminosities are achieved at this accretion rate because the radius of Jupiter is ∼50 times smaller than our fiducial one for the central protostar ($5\,{\rm R}_\odot$). With such extremely high luminosities, we can see that mass accretion simply cannot continue unabated without feedback playing some role. Our final clump masses and luminosities thus fall on the upper end of the range of expected values.

6 CONCLUSIONS

The primary motivation of this paper was to compare the evolution of an isolated and binary/multiple systems during the early stages of pre-stellar development within the same environment. Of particular interest was the potential for fragmentation of such early, accreting and self-gravitating discs. The following are our findings.

(i) The initial collapse occurs within filaments that tend to collimate infalling gas on to the central pre-stellar objects, whose specific angular momenta tend to remain aligned to that of the environment (and perpendicular to the embedding filament) on scales of ∼1000 au.

(ii) During formation, isolated systems must accrete mass and increase their specific angular momentum, leading to the formation of massive, extended discs, which undergo strong gravitational instabilities and are susceptible to fragmentation

(iii) In systems starting out as binaries and multiples, an effective specific angular momentum ceiling exists, limiting the maximum j of the systems but not their mass, making disc fragmentation unlikely. The ceiling is the product of tidal interactions which strip cold gas from members, and concentrate their mass profiles, and the redirection of angular momentum into orbits.

ACKNOWLEDGMENTS

The computations were performed in part on the Brutus cluster at the ETH Zürich, and the zBox2 and zBox3 supercomputers at the ITP, University of Zürich.

REFERENCES

Balsara D. S., 1989, PhD thesis, Univ. Illinois at Urbana-Champaign
Bate M. R., 1998, ApJ, 508, L95
Bate M. R., 2010, MNRAS, 404, L79
Bate M. R., Bonnell I. A., 1997, MNRAS, 285, 33
Bate M. R., Burkert A., 1997, MNRAS, 288, 1060
Bate M. R., Bonnell I. A., Bromm V., 2002, MNRAS, 336, 705
Bate M. R., Bonnell I. A., Bromm V., 2003, MNRAS, 339, 577
Boley A. C., 2009, ApJ, 695, L53
Boley A. C., Mejía A. C., Durisen R. H., Cai K., Pickett M. K., D'Alessio P., 2006, ApJ, 651, 517
Boley A. C., Hayfield T., Mayer L., Durisen R. H., 2010, Icarus, 207, 509
Bonnell I. A., 1994, MNRAS, 269, 837
Bonnell I. A., Bate M. R., 2006, MNRAS, 370, 488
Bonnell I. A., Bate M. R., Clarke C. J., Pringle J. E., 2001, MNRAS, 323, 785
Boss A. P., 1997a, ApJ, 483, 309
Boss A. P., 1997b, Sci, 276, 1836
Boss A. P., 2002, ApJ, 576, 462

Boss A. P., 2006, ApJ, 641, 1148
Boss A. P., 2008, ApJ, 677, 607
Burkert A., Bate M. R., Bodenheimer P., 1997, MNRAS, 289, 497
Commerçon B., Hennebelle P., Audit E., Chabrier G., Teyssier R., 2010, A&A, 510, L3
D'Alessio P., Calvet N., Hartmann L., 2001, ApJ, 553, 321
Dodson-Robinson S. E., Veras D., Ford E. B., Beichman C. A., 2009, ApJ, 707, 79
Duquennoy A., Mayor M., 1991, A&A, 248, 485
Durisen R. H., Gingold R. A., Tohline J. E., Boss A. P., 1986, ApJ, 305, 281
Eggenberger A., Udry S., Mayor M., 2004, A&A, 417, 353
Gingold R. A., Monaghan J. J., 1983, MNRAS, 204, 715
Haisch K. E., Jr, Lada E. A., Lada C. J., 2001, ApJ, 553, L153
Hennebelle P., Whitworth A. P., Cha S., Goodwin S. P., 2004, MNRAS, 348, 687
Kirk J. M., Ward-Thompson D., André P., 2007, MNRAS, 375, 843
Kratter K. M., Murray-Clay R. A., Youdin A. N., 2010, ApJ, 710, 1375
Krumholz M. R., McKee C. F., Klein R. I., 2005, Nat, 438, 332
Larson R. B., 1969, MNRAS, 145, 271
Larson R. B., 1981, MNRAS, 194, 809
Larson R. B., 1985, MNRAS, 214, 379
Low C., Lynden Bell D., 1976, MNRAS, 176, 367
Marois C., Macintosh B., Barman T., Zuckerman B., Song I., Patience J., Lafrenière D., Doyon R., 2008, Sci, 322, 1348
Marois C., Zuckerman B., Konopacky Q. M., Macintosh B., Barman T., 2010, Nat, 468, 1080
Masunaga H., Inutsuka S., 2000, ApJ, 531, 350
Mayer L., Quinn T., Wadsley J., Stadel J., 2004, ApJ, 609, 1045
Mayer L., Wadsley J., Quinn T., Stadel J., 2005, MNRAS, 363, 641
Mayer L., Lufkin G., Quinn T., Wadsley J., 2007, ApJ, 661, L77
Nayakshin S., 2010, MNRAS, 408, L36
Nelson A. F., 2000, ApJ, 537, L65
Nelson A. F., 2006, MNRAS, 373, 1039
Offner S. S. R., Klein R. I., McKee C. F., 2008, ApJ, 686, 1174
Pickett M. K., Durisen R. H., 2007, ApJ, 654, L155
Pickett B. K., Cassen P., Durisen R. H., Link R., 2000, ApJ, 529, 1034
Rafikov R. R., 2005, ApJ, 621, L69
Rafikov R. R., 2007, ApJ, 662, 642
Shen S., Wadsley J., Hayfield T., Ellens N., 2010, MNRAS, 401, 727
Stadel J. G., 2001, PhD thesis, Univ. Washington
Stahler S. W., Palla F., 2005, The Formation of Stars. John Wiley & Sons, Chichester.
Stamatellos D., Hubber D. A., Whitworth A. P., 2007, MNRAS, 382, L30
Tobin J. J., Hartmann L., Chiang H., Looney L. W., 2010, ApJ, 712, 1010
Tohline J. E., 1982, Fundamentals Cosmic Phys., 8, 1
Tomida K., Tomisaka K., Matsumoto T., Ohsuga K., Machida M. N., Saigo K., 2010, ApJ, 714, L58
Turner J. A., Chapman S. J., Bhattal A. S., Disney M. J., Pongracic H., Whitworth A. P., 1995, MNRAS, 277, 705
Vorobyov E. I., Basu S., 2007, MNRAS, 381, 1009
Vorobyov E. I., Basu S., 2010, ApJ, 714, L133
Wadsley J. W., Stadel J., Quinn T., 2004, New Astron., 9, 137
Walch S., Naab T., Burkert A., Whitworth A., Gritschneder M., 2010, MNRAS, 402, 2253
Whitehouse S. C., Bate M. R., 2006, MNRAS, 367, 32
Whitworth A. P., Chapman S. J., Bhattal A. S., Disney M. J., Pongracic H., Turner J. A., 1995, MNRAS, 277, 727

This paper has been typeset from a TEX/LATEX file prepared by the author.